Journal of Colloid and Interface Science 652 (2023) 2127–2138

Contents lists available at ScienceDirect

Journal of Colloid And Interface Science

journal homepage: www.elsevier.com/locate/jcis

Cooperative stiffening of flexible high aspect ratio nanostructures impart mechanobactericidal activity to soft substrates

Anindo Roy [a], Deepak Patil [a,b], Prasad K.D.V. Yarlagadda [c], Kaushik Chatterjee [a,*]

[a] Department of Materials Engineering, Indian Institute of Science, CV Raman Road, Bengaluru 560012, India
[b] Department of Production Engineering, National Institute of Technology, Tiruchirappalli, Tamil Nadu 620015, India
[c] School of Engineering, University of Southern Queensland, Springfield, QLD 4300, Australia

GRAPHICAL ABSTRACT

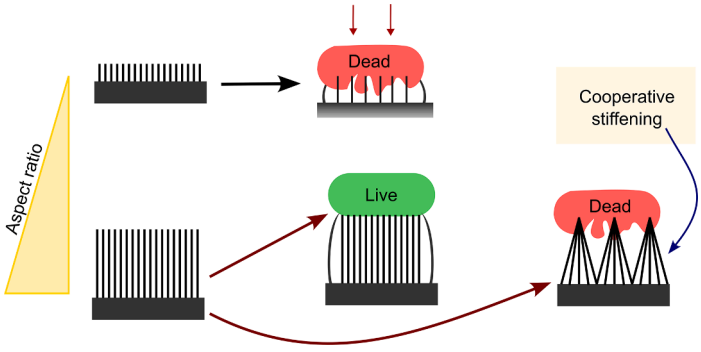

ARTICLE INFO

Keywords:
Antibacterial
Nanomaterials
Dry etching
Polymers
Surface engineering

ABSTRACT

Understanding how bacteria interact with surfaces with micrometer and/or sub-micrometer roughness is critical for developing antibiofouling and bactericidal topographies. A primary research focus in this field has been replicating and emulating bioinspired nanostructures on various substrates to investigate their mechano-bactericidal potential. Yet, reports on polymer substrates, especially with very high aspect ratios, have been rare, despite their widespread use in our daily lives. Specifically, the role of a decrease in stiffness with an increase in the aspect ratio of nanostructures may be consequential for the mechanobactericidal mechanism, which is biophysical in nature. Therefore, this work reports on generating bioinspired high aspect ratio nanostructures on poly(ethylene terephthalate) (PET) surfaces to study and elucidate their antibacterial and antibiofouling properties. Biomimetic nanotopographies with variable aspect ratios were generated via maskless dry etching of PET in oxygen plasma. It was found that both high and low-aspect ratio structures effectively neutralized Gram-negative bacterial contamination by imparting damage to their membranes but were unable to inactivate Gram-positive cells. Notably, the clustering of the soft, flexible tall nanopillars resulted in cooperative stiffening, as revealed by the nanomechanical behavior of the nanostructures and validated with the help of finite element simulations. Moreover, external capillary forces augmented the killing efficiency by enhancing the strain on the bacterial cell wall. Finally, experimental and computational investigation of the durability of the nanostructured surfaces showed that the structures were robust enough to withstand forces encountered in daily life. Our results

* Corresponding author.
E-mail address: kchatterjee@iisc.ac.in (K. Chatterjee).

https://doi.org/10.1016/j.jcis.2023.09.021
Received 8 May 2023; Received in revised form 5 August 2023; Accepted 4 September 2023
Available online 9 September 2023

demonstrate the potential of the single-step dry etching method for the fabrication of mechanobactericidal topographies and their potential in a wide variety of applications to minimize bacterial colonization of soft substrates like polymers.

1. Introduction

Nanostructured surfaces (NSSs) have garnered much attention over the past two decades due to their ability to impart functionality to surfaces by modifying how they respond to physical, chemical, and biological phenomena [1,2]. For example, NSSs can impart antireflective properties to a surface by manifesting a gradual change in refractive index from air to the bulk material [3], improve adhesive properties of a substrate via amplification of weak van der Waal's forces [4], and provide topological cues to cells for enhancing or reducing attachment [5]. It is often desirable for such surfaces to be multifunctional in nature, which can be achieved by tuning the dimensions of the nanostructures. Surface topography is also promising as a highly nonspecific method to tackle bacterial contamination and does not rely on small-molecule antibacterial compounds which promote antimicrobial resistance (AMR) [6]. AMR is widely acknowledged as a significant global threat and has now surpassed diseases such as HIV/AIDS and malaria in the death toll, globally accounting for more than 1.2 million deaths annually [7]. This rise in AMR, coupled with a dearth of novel antibiotics, now threatens to damage the advances in modern medicine by returning to the pre-antibiotic era [8,9]. However, while several studies have focused on generating such structures on hard materials, including ceramics and metals, fabrication on softer polymer surfaces has not been reported extensively [10–12]. This is especially surprising because polymer surfaces are ubiquitous in the modern age owing to the versatility in properties of polymer materials, along with their propensity to standardization at different length scales.

Bacterial colonization and infestation are especially consequential for industries such as food packaging and biomedical devices, where they can cause serious economic and human loss [13–15]. Ingesting bacterially contaminated foodstuffs can cause foodborne illness, and in the packaging industry, protection against microbes can potentially extend product shelf life and prevent contamination of perishable products such as meat and dairy [14,16]. In a nosocomial environment, several surfaces in rooms of infected patients, such as floors, bedside lockers, cardiac tables, and air exhaust vents, are at risk of contamination [17]. This can occur through direct touch by the patient or healthcare workers after contact with infected respiratory fluids, respiratory droplets emitted through coughing and sneezing, and respiratory aerosols [18–20]. Biofilm formation on indwelling medical devices is another growing concern that received additional attention after ventilator-associated pneumonia caused by *Pseudomonas* and *Staphylococci* species became prevalent in patients treated for COVID-19 [21–23]. Microbial contamination on such surfaces can remain viable for up to days suggesting food packets, clothes, transports, and building elements could also aid in spreading infection [14].

Researchers have devised several methodologies to combat these challenges, such as antibiotic-eluting surface coatings, bactericidal metal nanoparticle impregnation, and grafting of polymer brushes onto polymer surfaces [15]. However, one significant limitation of such chemical modifications is the specificity of the surface chemistry required for different polymer surfaces. Due to the unique surface chemistries of each polymer, specialized chemical modifications for each polymer application to achieve antibacterial effects can be challenging and add to the costs. Physicomechanical modifications, in contrast to chemical modifications, would be a promising alternative strategy because they could be used for a range of polymers. Bioinspired nanotexturing also features several advantages over other methods, including wide applicability against several bacterial strains, long shelf life, minimum post-implantation procedures, and minimal risk of AMR development. Plasma-based surface nanostructuring of polymers has been an active area of interest over the past decades with the possibility of tuning the wettability [24–26], improving or preventing adhesion, and applications in catalysis. Maskless dry etching, especially, has been demonstrated to be applicable to an incredibly broad range of materials, including ceramics, metals, composites, and several polymers [27]. Unlike patterned etching, maskless etching relies on the formation of micromasks inside the chamber. It hence does not require elaborate preprocessing such as precise patterning, curing, and washing steps, thereby reducing cost and time, which are key considerations for scale-up and widespread adoption in the industry. Furthermore, plasma treatment is already used in several applications, such as surface functionalization, cleaning, and/or improving adhesion or wettability. Thus, the industrialization of polymer nanostructuring processes using RIE can make bioinspired mechanobactericidal surfaces available for common usage.

Nanopatterned surfaces kill bacteria by eliciting significant deformation through contact, which is driven by intermolecular adhesion forces acting locally between the pillars and the bacteria [28]. This deformation may result in occasional death in a number of ways, ranging from relatively inconspicuous DNA, oxidative, or protein damage to highly pronounced physical rupture [28,29]. Such deformation necessitates the generation of large forces at the bacteria nanostructure contact and generates high stresses in the nanostructure, which will be consequential for soft and flexible substrates (especially as their aspect ratio increases), rendering them susceptible to bacterial colonization. Moreover, it has been previously reported that due to mechanoselective adhesion of bacteria, bacterial adhesion and biofilm growth on a soft, compliant nanostructured surface is inhibited as compared to a flat surface. [30]. To investigate this hypothesis, in this study, we selected poly (ethylene terephthalate) (PET), an important commercial polymer that has widespread use in the packaging, fiber, and biomedical industries. We fabricated bioinspired nanotopographies on PET substrates via maskless reactive ion etching using oxygen plasma and investigated the mechanism of the nanostructure formation process. Antibacterial assays and electron microscopy were used to investigate and understand differences in bacterial attachment between flat and nanostructured surfaces and the role of external capillary forces in the mechanobactericidal effect. Finite element simulations were used to elucidate the behavior of nanostructures under forces exerted by bacteria. Finally, we investigate the durability of such NSSs for practical purposes via experimental and computational approaches.

2. Materials and methods

2.1. Reactive ion etching of PET substrates

Biaxially stretched PET sheets, with a thickness of 150 μm, were used as polymeric substrates. Before experiments, the sheets were thoroughly washed using a detergent solution, followed by ethanol and deionized water to remove any surface contaminants, then air-dried overnight at room temperature. Clean PET samples were etched using oxygen (O_2) plasma inside a custom-built RIE plasma etching chamber equipped with a 13.56 MHz RF generator (Berthold, Germany) in a capacitively coupled (CCP) configuration. Nanotexturing was conducted using oxygen plasma struck by introducing 99.9 % purity oxygen into the reactor chamber via a showerhead, ensuring even gas distribution. The gas flow rate was controlled using a mass flow controller (Alicat Corporation, USA), and the pressure inside the chamber was maintained with the help of a turbomolecular pump (Edwards, UK) backed by a rotary vane pump

(HPVT technologies, India). The distance between the electrodes was maintained at 10 cm. Samples were placed on the lower electrode made of aluminum and etched using different recipes (Table 1).

2.2. Characterization of the nanotopographies

The nanotopographies generated on the polymer substrates were imaged using a scanning electron microscope (Ultra 55 FESEM, Carl Zeiss, Germany) after the deposition of a thin layer of gold using a sputtering system (JEOL, Japan) to avoid charging. At least three different regions were imaged for each sample to ascertain the uniformity of the structures across samples. Micrographs were captured at an operating voltage of 3 keV using a secondary electron detector.

The wettability of the flat and nanostructured sample surfaces was assessed using the sessile drop method with the help of a contact angle goniometer (OCA 15EC, Dataphysics, Germany). 8 μl of ultrapure MiliQ water (Sartorius, Arium) with a conductivity of 0.62 μS cm^{-1} was dispensed at a rate of 1 μl/s, under ambient conditions, and images were captured 2 s after dispensing. For each sample condition, the contact angle was measured at three different locations to understand the overall surface wettability.

The chemical composition of pristine and dry etched PET sheets was analyzed by Fourier transform infrared spectroscopy (FTIR) (Perkin Elmer Frontier IR/NIR systems, USA) in attenuated total reflectance mode. All IR spectra were recorded from 4000 cm^{-1} to 600 cm^{-1} with a resolution of 2 cm^{-1}. The signal-to-noise ratio was improved by co-adding 32 scans for each sample. All measurements were carried out at room temperature under ambient conditions.

Differential scanning calorimetry (DSC) scans were conducted to characterize the possible changes in the crystallinity of the polymer due to the etching process. Scans were conducted in the temperature range of 40 to 300 °C at a heating rate of 10 °C/min inside a DSC analyzer (TA instruments, USA). 4–5 mg of the sample were placed inside an aluminum container, and data from the first cooling and second heating curve were plotted.

The elemental composition of the pristine and plasma-treated PET surfaces was analyzed via X-ray photoelectron spectroscopy (XPS) (K-alpha, Thermo Scientific, USA) to determine changes induced by the etching process. The spectrometer was equipped with a monochromatic Al-Kα X-ray source (1486.3 eV) operating at a voltage of 12 kV and a beam current of 6 mA. The hydrocarbon component of the high-resolution C 1 s peak (binding energy 284.8 eV) was used as a reference for charge correction. Photoelectrons emitted from a circular area of 400 μm diameter were analyzed at 200 eV for survey spectra and then at 50 eV for region spectra. Wide spectra were recorded at 1 eV/step, whereas high-resolution spectra were recorded at 0.1 eV/step. Peak deconvolution, fitting, and analysis were performed using the Casa XPS software (ver. 2.3.22).

2.3. Mechanical characterization and durability of nanostructures

The mechanical reliability under touching and rubbing (i.e., normal and shear stress) and the resilience of the NT surfaces were investigated. The structural stability of the nanopillars under mechanical stress was evaluated by bending, twisting, vertically pressing, and horizontally rubbing the surface using a Universal Testing Machine (Model: Instron 5967). The external force was applied via a PDMS (Sylgard 184, Dow Corning, USA) block with a dimension of 1 cm × 1 cm × 1.5 cm. The block was placed on the nanostructured PET surface and slowly moved straight to the right while maintaining a pressure of 100 kPa. After exposure to these distinct types of mechanical stress, the structural damage to the NPs was observed and further analyzed by SEM.

Table 1
Process parameters for etch recipes used to fabricate the two nanotopographies investigated in this study.

Topography	RF power (W)	Gas flow rate (sccm)	Chamber pressure (mbar)
Nanopillars (T1)	30	40	0.05
Nanowires (T2)	60	60	0.05

The substrate temperature was maintained at 20 °C.

2.4. Bacterial culture conditions and assays

Stock solutions of Gram-negative *Pseudomonas aeruginosa* (ATCC 27853) and Gram-positive *Staphylococcus aureus* (ATCC 25923) were prepared in 20 % glycerol and stored at −80 °C until needed. Prior to experiments, stock solutions were refreshed on nutrient agar (HiMedia, India) plates, and a single bacterial colony was used to inoculate 5 ml of freshly prepared nutrient broth (HiMedia, India). This primary culture was then incubated overnight at 37 °C and 180 rpm and subsequently used to inoculate a secondary culture, which was allowed to grow till it reached the mid-logarithmic stage of growth (OD_{600} = 0.5). Bacterial suspensions were then diluted to a value of $OD6_{00}$ = 0.1 and used for all further experiments. OD values were measured using a spectrophotometer (Jenway Geneva Bio, Cole-Parmer, India).

2.4.1. LIVE/DEAD assay

The LIVE/DEAD assay was used to evaluate the possible damage to cell membranes included by the nanotopographies. Prior to experiments, flat and etched samples were washed using ethanol (99.9% pure) and copious amounts of deionized water followed by air-drying. Subsequently, they were exposed to UV radiation inside a laminar flow hood for 30 min on each side for sterilization. Then, a 20 μl droplet of bacterial suspension was deposited on the sample surfaces, and they were incubated at 37 °C for four hours in dark, static, and humid conditions. Post incubation, the excess suspension was discarded, and samples were gently washed three times using 1 ml of PBS (Sigma Aldrich, India) solution. The L7012 BacLight bacterial viability kit (Molecular Probes, Invitrogen, United States) was used to stain the cells following the manufacturer's protocol. The BacLight kit consists of a mixture of two nuclear and chromosome counterstains, namely SYTO 9 and PI, with an excitation/ emission maximum at 483/503 nm and 535/617 nm, respectively. SYTO 9 is permeable to cell membranes, whereas PI is non-permeant and, therefore, can only enter cells with damaged membranes. Samples were incubated with dye solution for 20 min and were then washed once using PBS to remove the excess dye. Microscopic image acquisition was performed using a confocal laser scanning microscope (Leica Falcon 9, Leica systems, Germany) using 20× (air) and 40× (oil) objectives. For each topography, at least three randomly chosen regions from three independent replicates were imaged, and counts of live and dead cells were quantified using the ImageJ software.

2.4.2. Colony forming unit (CFU) assay

The bactericidal activity of the nanostructured PET surface was examined with Gram-negative *P. aeruginosa* (ATCC 27853) using colony forming assay using a slightly modified ISO 22196 standard. Briefly, bacterial growth media was prepared by diluting nutrient broth (HiMedia, India) in autoclaved DI water (1:500). Bacteria were grown in 10 ml of this broth overnight at 180 rpm and 37 °C. Cells were then collected via centrifugation and diluted to a concentration of 10^5 cells/ml. The resulting bacterial suspension was further diluted 500-fold in sterile autoclaved deionized water reaching a final concentration of 10^3 cells/ml, for incubating the samples. Flat and nanostructured thin PET films with dimensions of 1.5 cm × 1.5 cm × 0.1 cm were washed using ethanol (99.9% pure) and ultrapure water (Sartorius, Arium) and subsequently exposed to UV light inside a laminar flow hood for 20 min on each side for sterilization. Samples were individually placed in a 90 mm radiation-sterilized plastic petri dish (Tarsons Products Limited, India) and inoculated with 10 μl of the bacterial suspension. A thin, sterile

Teflon film with a cross-section of 1 cm × 1 cm was placed on top and pressed down gently to ensure that the bacterial suspension spread out evenly throughout the sample surface and to minimize the drying of the bacterial suspension. The petri dishes were sealed using parafilm tape and then placed inside an incubator in a humid environment maintained at 37 °C for 24 h. Post-incubation, the samples were washed with 5 ml of sterile PBS to recover the cells, and serial dilutions of this wash solution were plated on nutrient agar plates. Colonies were counted after 24 h of incubation.

2.4.3. Bacterial morphology

The morphology of the bacterial cells was assessed by observing the samples with adhered cells inside an SEM (Ultra 55 FESEM Carl Zeiss, Germany). Prior to imaging, the cells were fixed using 2.5 % glutaraldehyde (SRL chemicals, India) solution for one hour and then serially dehydrated in 30, 50, 70, 90, and 100% ethanol and finally air-dried. The dried samples were gold coated (Quorum 150R, Quorum Technologies, United Kingdom) to prevent charge accumulation during imaging.

2.5. Finite element simulations

The nanomechanical behavior of individual polymer nanopillars was simulated under different loading conditions, including tangential shear loading and buckling. For simplicity, structures were modeled as 3D solid cylinders, and the pillar material was considered to be linear elastic, although PET is viscoelastic in nature. This is a fair assumption because at temperatures much below its glass transition temperature, the ratio of storage modulus to loss modulus ($\tan\delta$) for PET is very low [31], which means its behavior is largely elastic. The elastic modulus of the pillar was set to be 2.75 GPa, and Poisson's ratio was set to be 0.4 [31,32]. The pillar bottom was constrained in all dimensions. Compressive loading simulations were conducted by applying a pressure load to the top surface of the pillar. Non-linear buckling simulations were conducted in two steps. First, using a linear perturbation step, the pressure was applied on the top surface of the pillar, and the critical buckling load was calculated by multiplying the applied load with the eigenvalue for the first mode. Next, results from this step were used to simulate non-linear buckling by introducing imperfections in the material using Riks method in Abaqus. For shear loading simulations, the load was applied by defining a reference point at the pillar tip, which was kinematically coupled with the corresponding nodes on the top surface of the nanopillar. In the case of pillar clusters, five pillars inclined at twenty degrees were simulated, and tip displacements under shear load were calculated. The pillars were meshed using either hexagonal or tetrahedral geometry and assigned standard quadratic (C3D10 or C3D20) elements.

To assess the mechanical durability of the nanostructured substrates, sixteen pillars (4 × 4 grid) of T1 geometry were simulated on top of a PET cube. The pillars were connected to the bulk via a tie constraint, and interaction between the pillars was modeled as a general contact with rough tangential and hard normal formulations. The simulation was conducted in two steps, whereby normal pressure was applied via a PDMS block on top of the nanopillars in the first step, and shear was applied by assigning a tangential velocity to the block in the second step. All simulations were carried out using ABAQUS (ver. 2017) (Dassault Systems, France).

2.6. Statistical analysis

Data from LIVE/DEAD images were first tested for normal distribution using the Shapiro–Wilk normality test in Prism software (version 8.4.0, GraphPad, US). The Brown–Forsythe ANOVA test was then performed, followed by Dunnett's T3 multiple comparisons test to determine the statistical significance of the differences between the means of the different experimental groups.

3. Results and discussions

3.1. Mechanism and characterization of nanostructures

Flat PET sheets were subjected to dry etching using O_2 plasma inside a custom-built reactive ion etching chamber in a capacitively coupled configuration (see Supporting Information for a detailed description of the system). When exposed to the plasma, highly energetic ions present in the plasma are accelerated towards the polymer substrate. The generation of nanostructures involves both physical sputtering of the surface by the incoming ions as well as chemical reactions between the plasma species and the substrate surface. With the optimal gas composition, the chemical reaction between ions and the substrate atoms results in the production of volatile byproducts, which are pumped out of the reaction chamber as etching progresses. The exact mechanism of nanostructure formation is debatable but is broadly accepted to be attributable to inherent surface morphology [33] or co-deposition of metallic impurities during the etch process. We believe the formation of random nanoscale features can be ascribed to preferential etching by oxygen plasma directed by the co-deposition of metallic nanoparticles randomly sputtered from the cathode [34,35]. Such metal co-deposition results in the formation of micro-masks on the polymer surface, and the area directly beneath such masks have a slower etch rate than the pristine regions of PET. XPS analysis of the etched surface in our study shows the presence of the Al 2p peak, which is absent in the unetched surface, indicating the presence of sputtered Al nanoparticles, which is the same material as the lower cathode in our equipment (Fig. 1f). This process of micro-masking is reminiscent of the generation of nanopillars on titanium via SiO_xCl_y micro-masking, as reported by our group recently [36,37]. High aspect ratio nanoscale structures formed on the PET substrates with all recipes formulated for this study, albeit the characteristic nanoarchitectures differed from one another (Figure S1).

A range of values of three process parameters, namely chamber pressure, gas flow rate, and RF power, were initially tested to investigate the possibility of generation of high aspect ratio nanostructures and to identify trends exhibited with changes in these parameters (Figure S1). At relatively lower chamber pressures (0.03 mbar) the etch rate and anisotropic nature of etching increased, which resulted in many of the nanopillars getting etched out, whereas the remaining collapsed to form clusters at their tip, yielding tent-like formations. Conversely, at higher pressures, ion-ion collision is enhanced due to their increased residence time inside the chamber, especially in the sheath region, leading to deviation from their straight downward path, a suppression in kinetic energy, and a simultaneous increase in etch isotropy. This results in thinner and taller structures, with a greater tendency to collapse at the tip (Figs. S1, 1c).

In the case of platen power, which controls the dissociation percentage of the incoming gas (plasma density) and the ion kinetic energy, lower values (30 W) led to the generation of small pillar-like bumps (similar to the cicada wing surface). In contrast, increasing powers led to increases in pillar height and a decrease in pillar diameter, attributable to increased ion energy and density, respectively. At the actual low degrees of dissociation of only a few percent, the concentration of the reactive O radicals increases at constant RF power proportionally to the O_2 partial pressure. It causes the observed proportional increase in the etching rate. Finally, increasing gas flow rate (which determines ion residence time) led to an increase in etch isotropy, and structures formed at 60 sccm O_2 flow rate possessed nanowire-like morphology with tall, thin wires and evenly spaced tip clusters.

3.2. Effects of dry etching on physiochemical properties of the substrate and other emergent phenomena

Two distinct nanoarchitectures, a nanopillar (T1) and a nanowire (T2) topography, were chosen from this gallery of nanostructures generated herein to further study the effects of the dry etching process

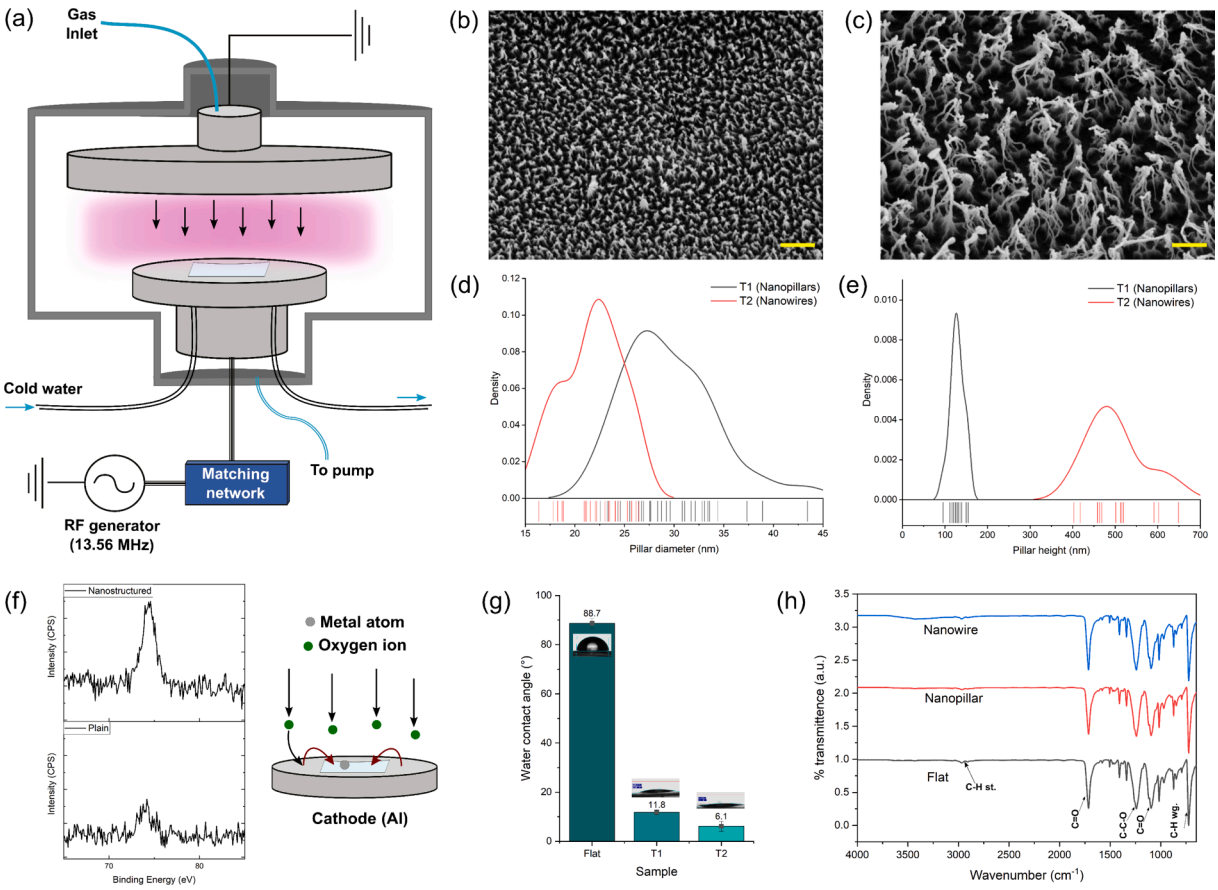

Fig. 1. (a) Schematic of the RIE chamber used in this study (b, c) FESEM micrographs of the two nanotopographies chosen for antibacterial assays; images were captured at an inclination of 15°. Scale bars are 500 nm. (d, e) Distribution + rug plots of nanostructure height and diameter for chosen topographies. (f) XPS spectra of Al 2p peak measured on flat and nanostructured samples; the presence of Al peak signifies that nanostructure formation occurs due to the polymer surface's micromasking by metal atoms sputtered from the cathode. (g) Water contact angle values as measured on flat, T1, and T2 surfaces, generation of nanostructures rendered the surfaces hydrophilic due to transition to Wenzel state. (h) FTIR spectra of flat unetched PET and T1 and T2 topographies did not show any changes in the chemical composition of the surface due to the etching process.

on the substrate, evaluation of antimicrobial activity, and gain insights into the bacteria nanostructure interaction mechanisms. Fig. 2(a, b) shows the inclined micrographs of the nanotopographies and the distribution of pillar diameter and heights. The pillar diameter for both samples was comparable at 21.7 ± 2.91 nm for T2 and 29.54 ± 4.57 nm for T1. This suggests that the size of sputtered metal micromasks is comparable under both etch recipes, and the marginal decrease noticed for T2 can be due to the higher kinetic energy of ions and, therefore, higher etch rate. In both cases, the broad distribution of pillar diameter is due to poor control over the size of the micromasks and their etch rates during a process run (Fig. 1d). The etched structures' height was 128.67 ± 15.39 nm and 501.4 ± 66.1 nm for T1 and T2, respectively (Fig. 1e), corresponding to etch rates of approximately 25.7 nm/min and 100.28 nm/min, respectively. The static water contact angle of the nanostructured topographies decreased to 11.8 ± 1° (T1) and 6.1 ± 2° (T2) from 88 ± 2° for the unetched PET surface. Thus, the nanopatterning of the substrates resulted in increased hydrophilicity and a transition from Young's state to Wenzel's wetting state. This transition can be attributed to an increase in the total surface area and roughness owing to high aspect ratio structures and the higher surface energy due to the creation of oxidized functionalities (=O and –OH groups) on the surface due to plasma exposure [38–40].

Another prominent feature is that the nanowires in T2 are not perfectly erect but seem to have collapsed into each other in a semi-erect, droopy arrangement. This is the result of the nanopillars bending laterally and adhering to their neighbors. Such lateral collapse can occur in high density arrays due to the small amount of bending energy required which can be easily compensated by the adhesion energy. The critical aspect ratio for lateral collapse due to interpillar interactions can be calculated as [41]

$$\left(\frac{h}{d}\right)_c = \left(\frac{3^{3/4}\pi E w^{3/2}}{2^{1/4}32\gamma_{sv}(1-\nu^2)^{1/4}d^{1/2}}\right)^{1/3}$$

where, h, d are the height and diameter of the structures, E and ν are the elastic modulus and Poisson's ratio of the material, respectively, and γ_{sv} is the surface energy of the substrate and w is the interspacing. The elastic modulus, Poisson's ratio, and surface energy for the substrate are assumed to be 2.75 GPa, 0.4, and 0.042 N/m, respectively [31,32]. For the pillar dimensions of T2, the critical interspacing is 15.79 nm, suggesting the pillars are unstable and should collapse to form tip clusters, as observed from the SEM micrographs, which results in the formation of tent-like superstructures.

FTIR was used to investigate the chemical bonds in the material and any possible changes induced by exposure to plasma etching. The FTIR spectra for unetched PET and nanopillar and nanowire topographies are shown in Fig. 1h, and the list of bonds associated with the observed peaks is provided in Table S1 (see Supporting Information). No differences were observed in the spectra of the fat and the nanostructured samples, demonstrating that the dry etching process did not affect the chemical characteristics of the samples. The other polar groups that form on the NSSs post-etching do not appear in the FTIR spectra because these bonds (–OH, C=O, and –COOH) are intrinsic to the PET structure.

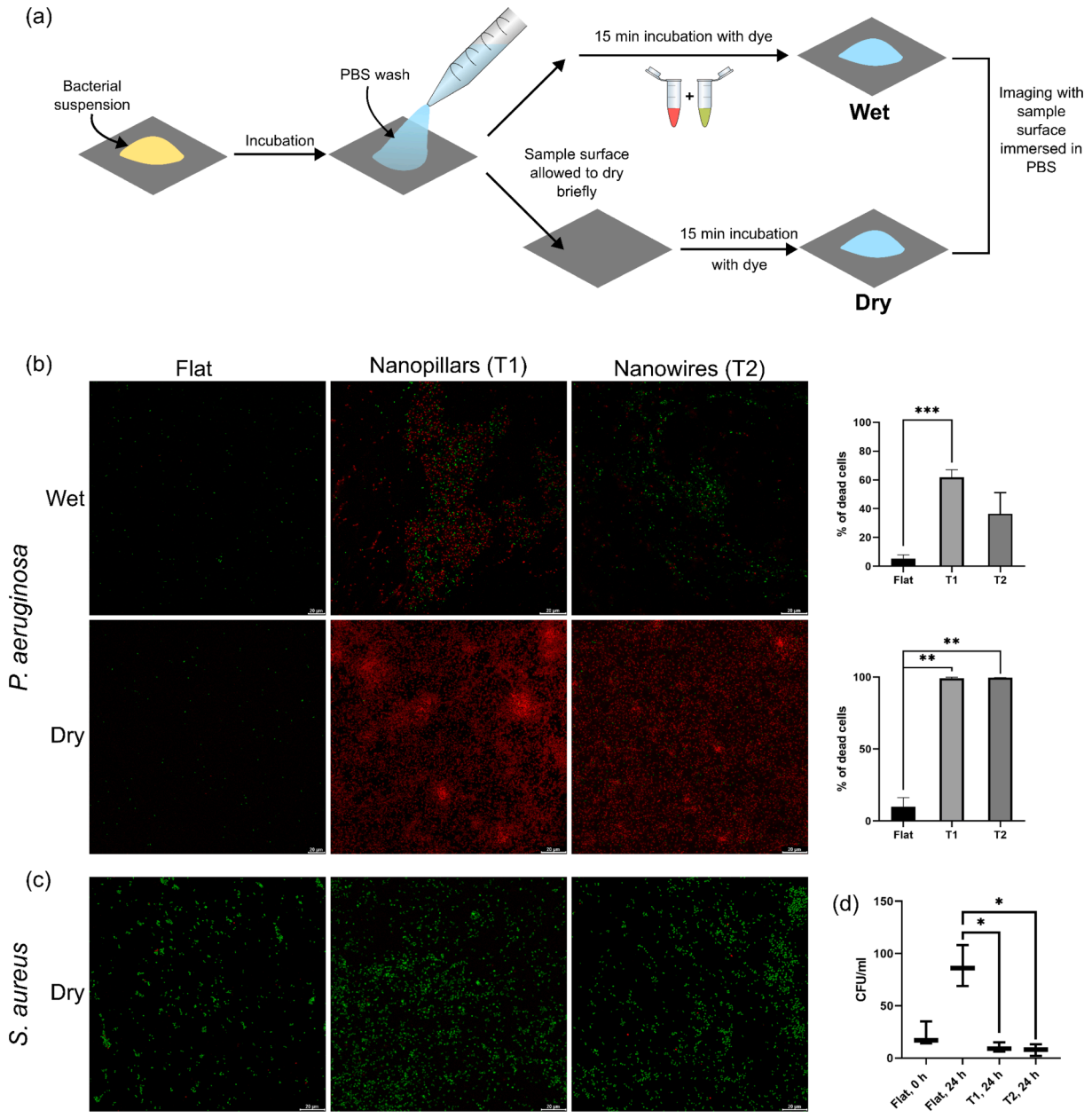

Fig. 2. (a) Schematic of steps to evaluate antibacterial activity via live/dead assay. (b) Fluorescence micrographs of P. aeruginosa on flat, T1 and T2 surfaces in "wet" and "dry" condition. (c) Fluorescence micrographs of S. aureus on flat, T1 and T2 in "dry" condition. Scale bars are 20 μm. The adjacent bar graphs on the right show percentage of dead cells quantified from the fluorescence micrographs. (d) Colony forming units (CFU)/ml of P. aeruginosa cells retrieved from different samples. *p < 0.05, **p < 0.005, ***p < 0.001. Data are shown as mean ± S.D. for n = 3.

Moreover, peaks representative of both crystalline and amorphous regions are present in the spectra, confirming the semi-crystalline nature of the sample. Biaxially stretched semi-crystalline PET substrates, as used in this study, are known to have a three-phase composition of amorphous, ordered amorphous and crystalline phases. DSC studies further showed that the semi-crystalline nature of the sample was not affected by the dry etching treatment (Figure S2). However, the degree of crystallinity of the polymer can affect the nanostructure morphology generated via maskless etching. Studies have shown that the degree of crystallinity of semi-crystalline samples changes marginally (by 0.2%) due to the etching process, similar to what we found in this study [42]. This is expected since the plasma etching acts only on the surface region, with low penetration depth. Moreover, during the etching process, the crystallinity of the substrate is largely preserved because the penetration depth of the ions is much smaller than the lateral dimensions of the etching inhibitors [39,42].

3.3. *External capillary forces augment the mechanobactericidal activity of polymer nanostructures*

It is now well-accepted that nanostructured surfaces can kill bacteria or reduce their attachment by straining/deforming the cell wall leading to rupture and/or disturbing critical intercellular processes such as protein synthesis or reactive oxygen species levels [28,43]. Moreover, previous studies have consistently found differences in bactericidal efficacy against Gram-positive and -negative bacteria attributed to differences in their cell wall structure [44]. Therefore, flat and etched topographies were tested against two well-known pathogenic bacteria, the Gram-negative *P. aeruginosa* and Gram-positive *S. aureus,* to evaluate and quantify their mechanobactericidal activity and elucidate the

underlying mechanism of action. Drug-resistant strains of both these bacteria have been identified globally and are responsible for various infections, including severe respiratory infections of cystic fibrosis patients in the case of *P. aeruginosa* and post-implant colonization of surfaces for *S. aureus*. Initial experiments were performed on "wet" surfaces, i.e., all the post-incubation steps, such as PBS washing and staining, were conducted carefully without allowing the sample surface to dry completely. Results showed that while both T1 and T2 were bactericidal, nearly 50% of cells on both surfaces were still alive. More recent research has suggested that external capillary forces exerted on the cells due to movement of the air–liquid interface play a role in determining their bactericidal efficacy [45,46]. It is believed that as the liquid evaporates, the surface tension of the liquid manifests as capillary bridges, which exert an extra downward pull on the cells, augmenting the stresses generated in the cell wall. Therefore, in another set of experiments, the sample surface was allowed to dry briefly for 10–15 s before being immersed in PBS again for imaging (Fig. 2a). Fluorescence micrographs then showed that both the topographies were highly bactericidal (>99% dead cells) compared to the flat PET substrate, where most cells were viable. In the case of Gram-positive *S. aureus*, there were no differences between the flat and NSSs, even in the "dry" state. This is attributed to the thick peptidoglycan layer of *S. aureus* which makes it more resistant to wall deformation and rupture.

The high killing efficacy of the T2 surface was puzzling at first because of the high aspect ratio of the structures and their low mechanical rigidity, as is evident from SEM micrographs. However, electron micrographs with bacterial cells revealed several tip clusters formed via the clustering of several pillars in a tent-like arrangement (Fig. 3). Indeed, similar clustering of nanopillars due to the action of capillary forces has been reported previously [41,47]. This clustering is responsible for the increased cooperative rigidity of the structures and subsequently explains the high killing efficacy when the sample was allowed to dry briefly, allowing capillary forces to act, whereas, on the wet sample, the number of dead cells was significantly lower. Though

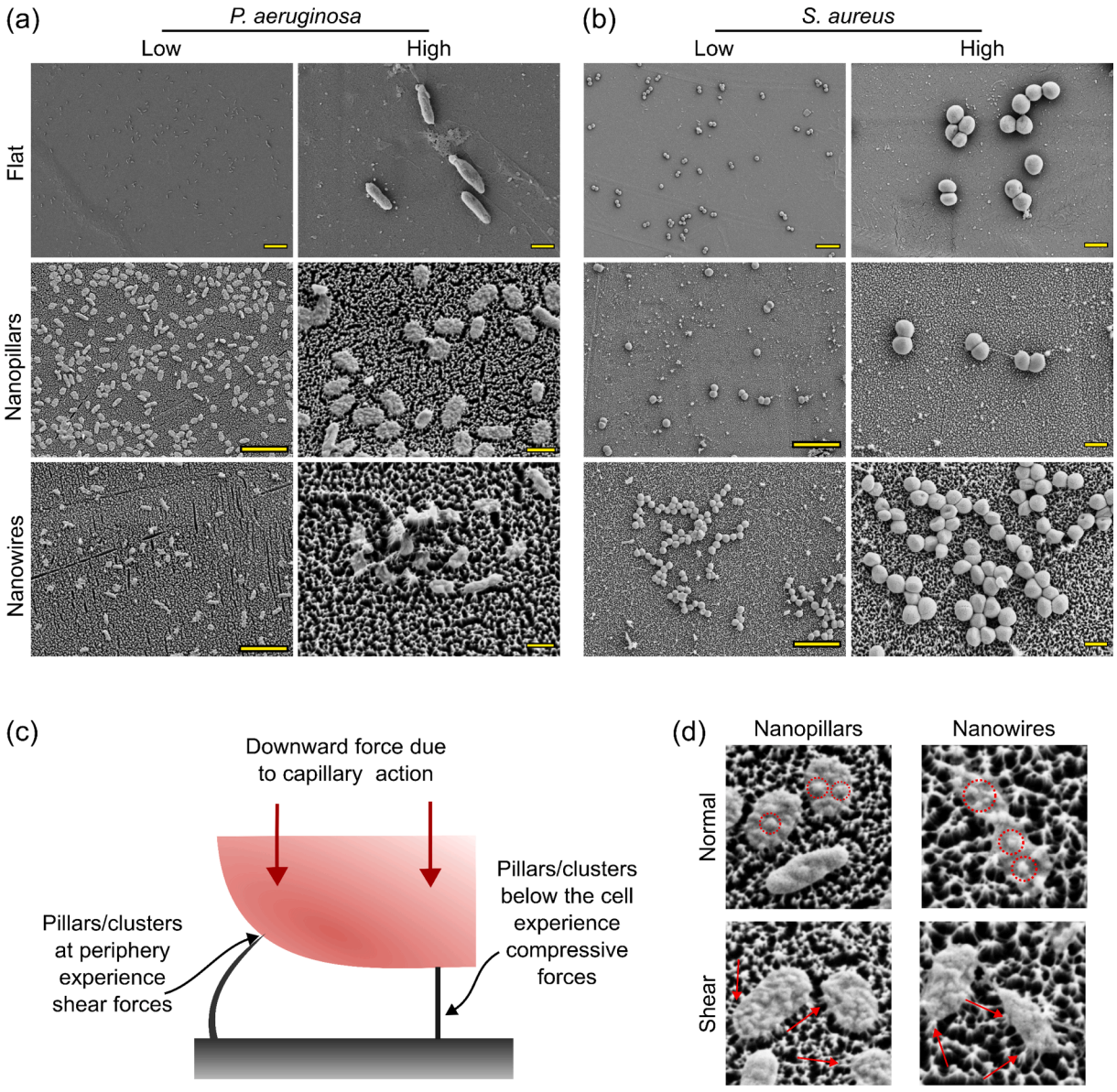

Fig. 3. High and low magnification SEM micrographs of (a) P. aeruginosa and (b) S. aureus on flat and NSSs Cell wall deformation of P. aeruginosa is clearly visible on the nanostructured topographies, while the attachment of bacteria to the tips of nanostructures is clearly visible for both strains. Scale bars are 5 μm (low mag) and 1 μm (high mag). (c) Schematic representation of differences in the nature of forces experienced by nanostructures depending on their relative position against the bacterial cell. (d) SEM micrographs showing pillar/cluster tips penetrate through the cell when located directly beneath the cell and undergo bending deformation when located at the periphery.

lateral adhesion has been reported in high–aspect ratio structures such as arrays of carbon nanotubes, and biomimetic setal adhesives, it is often considered an unwanted outcome that leads to the uncontrolled collapse of the structures. Contrarily, in the case of bactericidal nanostructures, the clustering process resulted in organized assemblies, which can be useful to enhance the mechanobactericidal activity of soft HAR nanostructures.

Plasma treatment also increases surface free energy, which leads to an increase in the work function, or the energy barrier a bacterial cell must overcome to irreversibly attach to the substrate [48] while rendering the surface hydrophilic. Valiei *et al.* have shown that the enhancement of bactericidal killing efficiency by external capillary forces is more pronounced in the case of hydrophilic surfaces due to the tendency of the liquid to form a thin film and, consequently, have faster evaporation rates [45]. In this study, the increased total surface area also plays a role in determining adhesion for hydrophilic surfaces, such as T1 and T2 topographies. Micropatterned polymer surfaces, especially with trenches smaller than the cell body, can prevent bacterial colonization through entrapment of air bubbles between surface features, but are susceptible to increased adhesion and colonization at longer time scales, once the surface becomes completely wettable or via the action of surface appendages such as flagella [49,50].

The morphology of the bacterial cells was further investigated using SEM, and the results corroborated findings from the live/dead assay. The cell wall integrity of *S. aureus* cells appears intact on the flat and nanostructured surfaces, and the bacteria seems to be in the early stages of microcolony formation (Fig. 3b). For *P. aeruginosa*, cells were undamaged and found to adhere successfully on the flat surface. Damage to the cell wall of *P. aeruginosa* is clearly visible on T1 and T2 surfaces, confirming that the nanostructures impaled the cells, which induced cell death. Especially in the case of T1, the cell wall is seemingly compromised at the point of bacteria-nanostructure contact, and for some cells, pillar tips are clearly visible through the bacteria (Fig. 3a). The adhesion forces on NSSs are lower than those on flat surfaces due to the lower contact area available for attachment, as the contact between a cell and a surface is mediated primarily by cell wall macromolecules tethering to the substrate [51]. Bacteria attach to a surface over distances of ≈50 nm (far beyond the range of classical forces) via stochastic binding of thermally fluctuating cell wall proteins [52]. Finite element simulations of Gram-negative bacteria interacting with nanopillars have found that the critical action site or the part of the bacterial envelope that experiences maximum strain is at the pillar tip [29].

Moreover, because interaction forces develop individually at each pillar tip and not uniformly throughout the cell wall, pillars are “pulled” into contact specifically at the periphery of cells (Fig. 3a). Thus, during the action of the capillary force, the pillars directly beneath the bacterial cell experience a compressive load, while those at the periphery experience a shear pull. This shear force at the pillar tip causes the bending of the pillar in the direction of the bacteria (Fig. 3c), and the compressive load can cause the failure of the structure via buckling. Buckling instabilities are more pronounced in structures with higher aspect ratios, and if it does indeed occur, it would severely impair the ability of the structure to deform and penetrate the cell wall.

To further validate this hypothesis, we investigated the compressive, shear deformation and buckling behavior of T1 pillars and T2 pillar clusters via FEM simulations (Fig. 4). Using Euler’s theory for buckling of ideal elastic columns, T1 will undergo compressive yielding before buckling, whereas T2 will fail via buckling (see Section 2.6, Supplementary Information). The compressive behavior of T1 was simulated by applying a 100 nN load at the pillar apex (Fig. 4a), and it was found

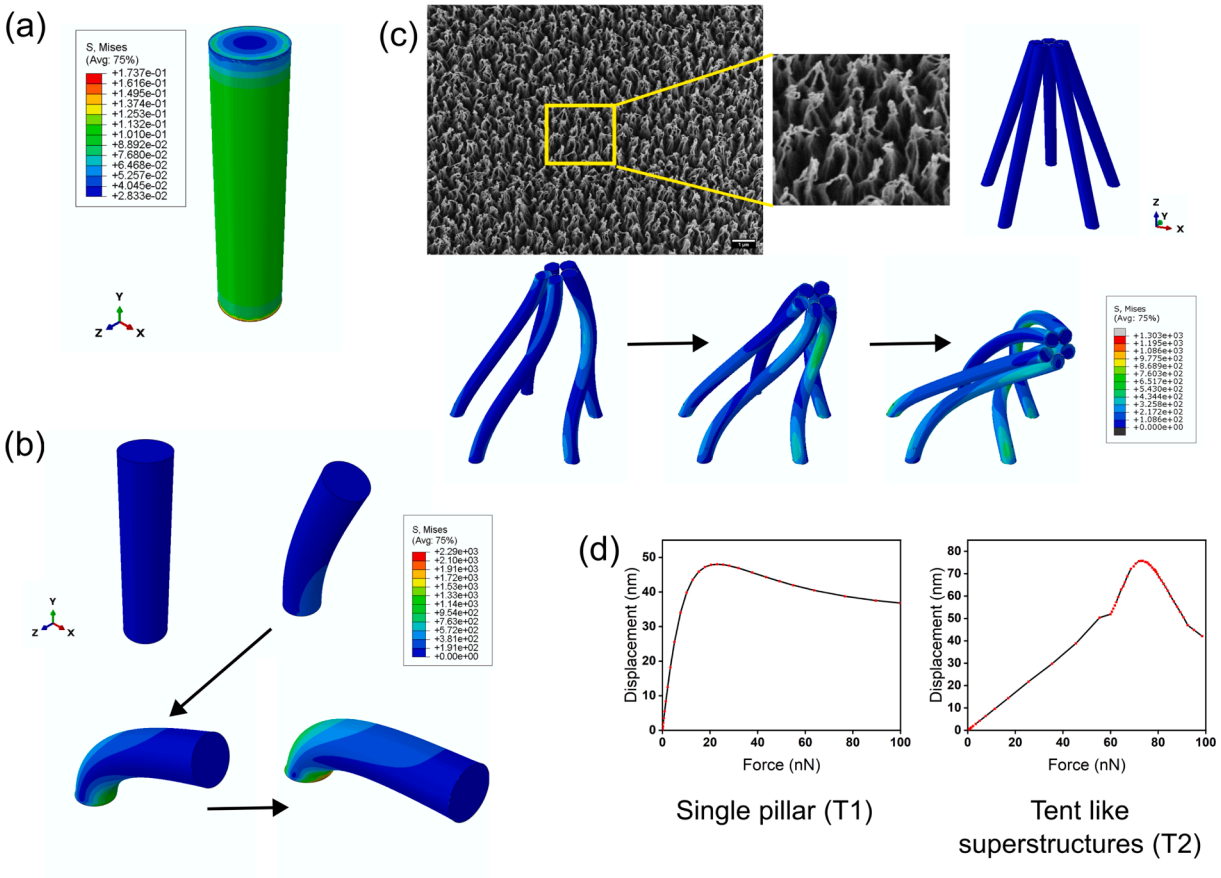

Fig. 4. FEM simulation of (a) compressive loading of T1. (b, c) Deformation behavior of (b) T1 nanopillars and (c) T2 nanopillar clusters under shear loading at the tip. (d) Displacement vs. force curves for T1 (upper) and T2 clusters (lower). Stresses are represented in MPa.

that the pillar remains stable, with maximum stress in the pillar reaching 173.7 kPa. There is minimal distortion/ compression of the pillar as well, indicating that T1 behaves as a rigid body, even under forces orders of magnitude higher than those exerted during capillary action. This is expected because the pillar has a relatively low aspect ratio of 4.34. The buckling load for a single T2 nanopillar is calculated to be 1.74 nN using Euler's formula and 3.03 nN using non-linear buckling analysis in ABAQUS. Valiei *et al.* calculated that during passage of the air–liquid interface, the peak force can reach 200–250 nN (for a bacteria 15 μm long and 500 nm in width) [46] which is distributed amongst the pillars directly beneath it. Thus, depending on pillar density, T2 structures can buckle under such loading and fail to rupture the bacterial cell wall. However, as noticed in our study, formation of tent-like superstructures consisting of these pillars provides them with enhanced rigidity allowing them to maintain their mechanobactericidal action.

In the case of shear loading, a force from 0 to 100 nN was applied at the tip of the pillar/cluster (Fig. 4 (b, c)), and the corresponding force–displacement curves were obtained from the simulations (Fig. 4d). In the case of T1, the deflection of the pillar tip increases monotonously with force at the tip up to a force of ≈30 nN. Beyond this point, pillar bending continues, and stress at the tip increases, but the magnitude of tip deflection decreases a little, possibly due to excessive bending of the pillar while the pillar bottom is fixed. For the T2 topography, a cluster of five pillars was simulated like those observed in SEM micrographs. The simulated morphology matches well with the deflected clusters observed in SEM micrographs of bacteria atop the T2 surface, and the F-D curve reveals that tip deflection is initially linear, like T1, up to a certain force (~60 nN). Beyond this force, deflection abruptly increases and then decreases, possibly due to excessive bending of the structure.

Although the LIVE/DEAD staining protocol helps determine a surface's antibacterial potential and allows observation of cell wall integrity, some recent studies have suggested that it might not be sufficient for quantitatively evaluating the mechanobactericidal activity of nanostructured surfaces. This is primarily for two reasons. First, quantitative evaluation based on such micrographs might be misleading because the field of view on a fluorescence micrograph is very limited compared to sample sizes (tens or hundreds of μm^2 vs. several cm^2). And secondly, the rinsing and staining steps involved in the sample preparation might exert shear and capillary forces, which can dislodge cells from surfaces or push them onto the nanostructures, as observed in this study. Therefore, we also evaluated the antibacterial activity of all three surfaces via the colony count method, using a modified ISO protocol prescribed for evaluating the contact-killing antibacterial efficacy of plastic surfaces [53,54]. On a flat substrate, the CFU count increased from 22 at 0 h to 87.67 after 24 h incubation, indicating bacteria could survive and thrive on these surfaces. Contrarily, bacterial count decreased on both T1 (3.74) and T2 (4.49) surfaces after 24 h, reinforcing results from the LIVE/DEAD assay and SEM micrographs (Fig. 2d).

Therefore, our results show that both low and high aspect ratio polymer nanostructures can be bactericidal and that external capillary forces are indispensable in exacerbating the mechanobactericidal nature of NSSs. Recent studies have also shown that external forces normally applied to the surface via other methods, such as centrifugation of the NSSs with adhered bacteria, can also improve the damage to the cell wall or kill activity manifolds [55,56]. Bacteria on jagged topographies can also be vulnerable to high levels of oxidative stress, changes in protein expression, and reduced metabolic activity even when they might not be completely lysed [57]. Thus, the bactericidal mechanism might be multifaceted, with several factors concurrently acting toward reduced bacterial survival on nanostructured topographies [28]. Lastly, while the NSSs can successfully eliminate Gram-negative pathogens, Gram-positive pathogens can attach to and survive on these surfaces. However, this limitation can be solved by using NSSs in conjunction with preservative agents like nisin, which are well-known for their excellent bactericidal activity against Gram-positive strains [58]. Furthermore, it has also been demonstrated that bacteria on nanostructured surfaces have an increased susceptibility to antibiotics and, therefore, can be useful in fighting AMR through the use of lower doses, over shorter durations [59].

3.4. Durability of nanopillars under mechanical loading

Surfaces used in food processing, packaging applications, and protective coverings can be exposed to distinct types of stresses, including mechanical (abrasion, shear), chemical (acidic, alkaline), and thermal (steam, freezing). For touch surfaces, long-term durability and the ability to resist damage under small loads (e.g., the pressure exerted by human touch) are crucial for practical applicability. Thus, we evaluated the mechanical stability of etched nanostructures under external forces by subjecting the etched topographies to 100 kPa pressure, which is the typical force applied by hand on phone screens or while working with tools. The T1 topography was selected for mechanical testing and was exposed to normal and shear forces via a solid PDMS block, mimicking human touch. Fig. 5(a and b) show the representative SEM micrographs of nanopillar before and after applying normal and shear forces, respectively. The micrographs show that the nanostructures were not distorted or damaged after normal loading and retained their original topographical characteristics. However, under shear forces, some pillars appear to deform marginally in the direction of shear. The T1 sample was also subjected to bending and twisting forces. In both cases, several cracks appeared on the samples, and the interspacing increased marginally, although the pillars themselves appear to have suffered minimal distortion (Fig. 5b). Therefore, the O_2 plasma etched nanostructures are mostly resilient to forces of small magnitude, physical abrasion, and torsion that might be experienced during daily handling.

We further simulated the normal compression and shear deformation of the pillars with the PDMS block using FEM to understand their durable nature better. As shown in Fig. 5c, the initial setup consisted of sixteen nanopillars of T1 geometry on a bulk PET substrate. A PDMS block was used to apply downward pressure and then translated along the surface in a subsequent step, like in our experiments. Simulations reveal that compressive loading using 0.1 MPa pressure generated stresses of the order of 15 MPa at the pillar base, which is much lower than the reported yield strength values for PET (~50 MPa). This supports the experimental observation that the nanostructures remain largely unaffected by normal forces. Stresses further increased to values as high as 185 MPa during the application of subsequent shear steps, as pillar tips deflect in the shear direction. Therefore, based on simulations and experimental observations, we conclude that mechanobactericidal nanostructures are most susceptible to damage under a combination of normal and shear loading. Normal loading imparts minimal damage, whereas bending or twisting leads to the formation of sub-micron cracks, but neither damages the nanostructures themselves. Durability under shear loading could be possibly improved either by using materials with superior mechanical properties (higher yield strength) or by ensuring that the surface is not exposed to shear loading at high pressures.

4. Conclusions

In this study, we demonstrated that dry etching of PET surfaces could be a rapid, robust, and effective route for the generation of bioinspired nanostructures with tunable dimensions. The treatment of PET with RF discharge oxygen plasma at low pressures leads to the generation of nanostructures whose morphology and dimensions can be modulated through control over a set of process parameters. Experiments showed that high aspect ratio pillars exhibit tip clustering forming tent-like superstructures, which results in the stiffening of the structures and makes them less susceptible to deformation. Therefore, aspect ratio-dependent emergent physical phenomena play a dominant role in determining the bactericidal efficacy of soft materials such as polymer nanostructures. Moreover, the mechanobactericidal activity is significantly augmented by the action of external capillary forces, which exert a downward force

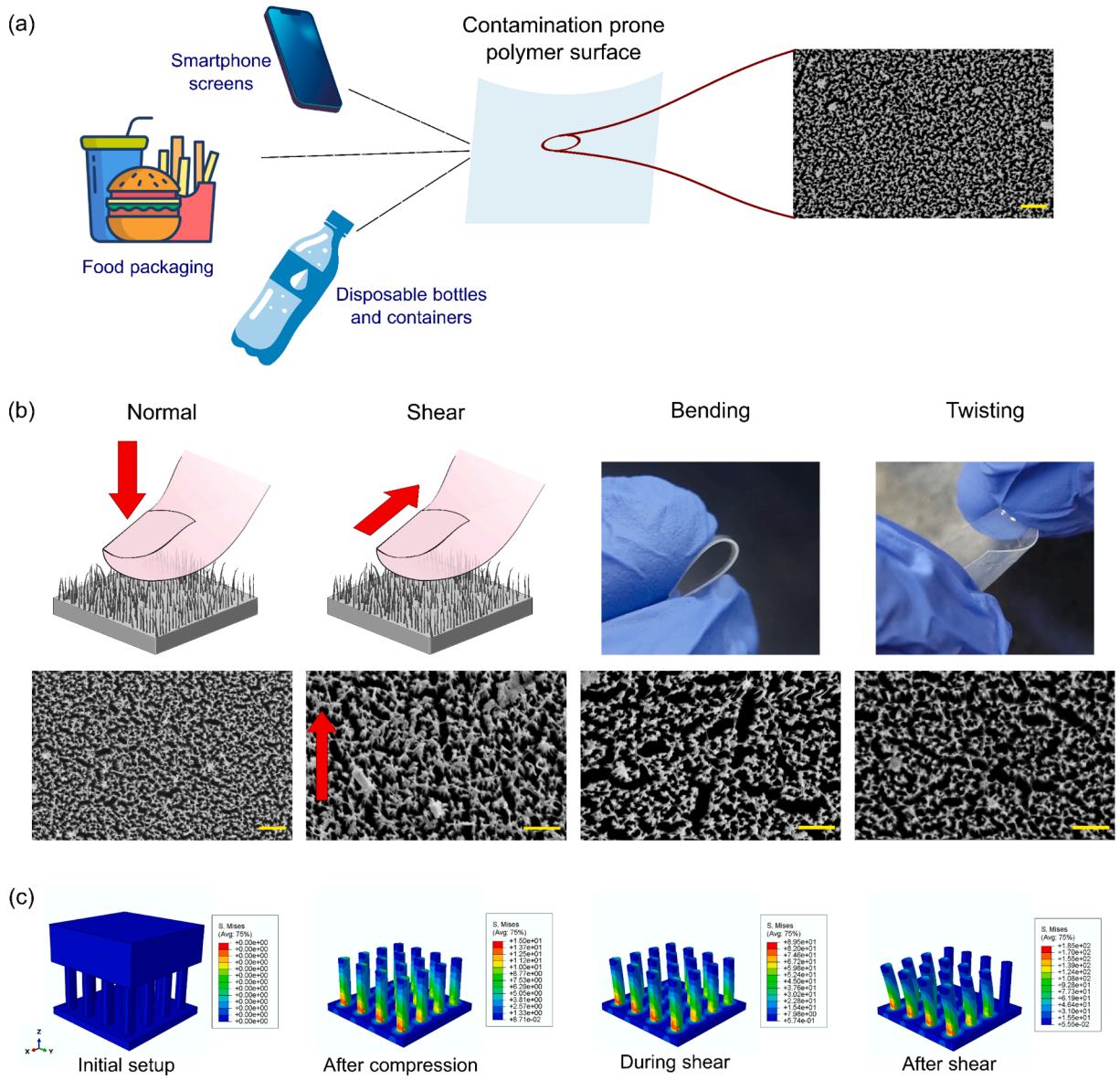

Fig. 5. (a) Schematic of different applications of polymers where they are prone to contamination and spreading of infections; the SEM micrographs on the right show the nanostructured PET surface before loading. (b) Scanning electron micrographs (SEM) of nanostructured PET sheet after normal loading at 100 kPa, shear loading, bending, and twisting. Scale bars are 1 μm. (c) FEM simulations of compressive and shear loading of the nanostructured surface (T1 geometry) at different process stages. Stresses are represented in MPa.

on the cells, pushing them onto the nanostructures and impaling them in the process. Theoretical calculations and finite element simulations reveal that whereas individual high aspect ratio pillars may be susceptible to failure via buckling under the compressive forces exerted by the bacteria, the formation of tent-like superstructures endows them with enhanced rigidity, thereby allowing them to maintain mechanobactericidal activity. Pillars on the cell periphery undergo bending deformations due to shear pull exerted at the tip, which is adhered to the cell and contribute little toward cell wall rupture. Mechanical testing and FEM simulations demonstrated that the nanostructures were durable enough to be used in daily applications such as touch surfaces and packaging material. These findings demonstrate that mechanobactericidal effect of soft material nanostructures can manifest in ways fundamentally different than metallic or ceramic materials and are important to consider for the fabrication of multifunctional surfaces.

CRediT authorship contribution statement

Anindo Roy: Conceptualization, Methodology, Investigation, Software, Validation, Formal analysis, Writing – original draft, Visualization. **Deepak Patil:** Methodology, Investigation, Validation, Writing – review & editing. **Prasad K.D.V. Yarlagadda:** Supervision, Writing – review & editing, Funding acquisition. **Kaushik Chatterjee:** Conceptualization, Resources, Writing – review & editing, Supervision, Project administration, Funding acquisition.

Declaration of Competing Interest

The authors declare that they have no known competing financial interests or personal relationships that could have appeared to influence the work reported in this paper.

Data availability

Data will be made available on request.

Acknowledgments

The authors thank Mr. Pritiranjan Mondal for his help with the FTIR characterization. This work was funded by the Department of Science and Technology (DST), Government of India (DST/AISRF/2020/54). PKDVY acknowledges VAJRA Professorship from the Science and Engineering Research Board, Government of India.

Appendix A. Supplementary data

Supplementary data to this article can be found online at https://doi.org/10.1016/j.jcis.2023.09.021.

References

[1] J. Hasan, A. Roy, K. Chatterjee, P.K. Yarlagadda, Mimicking insect wings: the roadmap to bioinspiration, ACS Biomater Sci. Eng. 5 (7) (2019) 3139–3160.
[2] S.G. Moghadam, H. Parsimehr, A. Ehsani, Multifunctional superhydrophobic surfaces, Adv. Colloid Interface Sci. 290 (2021), 102397.
[3] S. Kim, U.T. Jung, S.-K. Kim, J.-H. Lee, H.S. Choi, C.-S. Kim, M.Y. Jeong, Nanostructured multifunctional surface with antireflective and antimicrobial characteristics, ACS Appl. Mater. Interfaces 7 (1) (2015) 326–331.
[4] W. Duan, Z. Yu, W. Cui, Z. Zhang, W. Zhang, Y. Tian, Bio-inspired switchable soft adhesion for the boost of adhesive surfaces and robotics applications: A brief review, Adv. Colloid Interface Sci. 102862 (2023).
[5] S.G. Higgins, M. Becce, A. Belessiotis-Richards, H. Seong, J.E. Sero, M.M. Stevens, High-Aspect-Ratio nanostructured surfaces as biological metamaterials, Adv. Mater. 32 (9) (2020) 1903862.
[6] D.P. Linklater, E.P. Ivanova, Nanostructured antibacterial surfaces–What can be achieved? Nano Today 43 (2022), 101404.
[7] C.J. Murray, K.S. Ikuta, F. Sharara, L. Swetschinski, G.R. Aguilar, A. Gray, C. Han, C. Bisignano, P. Rao, E. Wool, Global burden of bacterial antimicrobial resistance in 2019: a systematic analysis, Lancet 399 (10325) (2022) 629–655.
[8] A. Catalano, D. Iacopetta, J. Ceramella, D. Scumaci, F. Giuzio, C. Saturnino, S. Aquaro, C. Rosano, M.S. Sinicropi, Multidrug resistance (MDR): A widespread phenomenon in pharmacological therapies, Molecules 27 (3) (2022) 616.
[9] S. Reardon, WHO warns against 'post-antibiotic'era, Nature 15 (2014) 135–138.
[10] J. Shen, D. Guercio, I.L. Heckler, T. Jiang, S.T. Laughlin, E.M. Boon, S.R. Bhatia, Self-Patterned nanoscale topography of thin copolymer films prepared by evaporative Assembly-Resist Early-Stage bacterial adhesion, ACS applied bio materials 5 (8) (2022) 3870–3882.
[11] S.C. Lohmann, A. Tripathy, A. Milionis, A. Keller, D. Poulikakos, Effect of flexibility and size of nanofabricated topographies on the mechanobactericidal efficacy of polymeric surfaces, ACS Applied Bio Materials 5 (4) (2022) 1564–1575.
[12] D.P. Linklater, S. Saita, T. Murata, T. Yanagishita, C. Dekiwadia, R.J. Crawford, H. Masuda, H. Kusaka, E.P. Ivanova, Nanopillar polymer films as antibacterial packaging materials, ACS Applied Nano materials 5 (2) (2022) 2578–2591.
[13] F. Cappitelli, A. Polo, F. Villa, Biofilm formation in food processing environments is still poorly understood and controlled, Food Eng. Rev. 6 (2014) 29–42.
[14] W. DeFlorio, S. Liu, A.R. White, T.M. Taylor, L. Cisneros-Zevallos, Y. Min, E. M. Scholar, Recent developments in antimicrobial and antifouling coatings to reduce or prevent contamination and cross-contamination of food contact surfaces by bacteria, Compr. Rev. Food Sci. Food Saf. 20 (3) (2021) 3093–3134.
[15] E.L. Meier, Y. Jang, Surface design strategies of polymeric biomedical implants for antibacterial properties, current opinion, Biomed. Eng. (2023), 100448.
[16] S. Zouaghi, S. Bellayer, V. Thomy, T. Dargent, Y. Coffinier, C. Andre, G. Delaplace, M. Jimenez, Biomimetic surface modifications of stainless steel targeting dairy fouling mitigation and bacterial adhesion, Food Bioprod. Process. 113 (2019) 32–38.
[17] A.F. Monegro, V. Muppidi, H. Regunath, Hospital acquired infections, StatPearls [Internet], StatPearls Publishing, 2022.
[18] P.Y. Chia, K.K. Coleman, Y.K. Tan, S.W.X. Ong, M. Gum, S.K. Lau, X.F. Lim, A. S. Lim, S. Sutjipto, P.H. Lee, Detection of air and surface contamination by SARS-CoV-2 in hospital rooms of infected patients, Nat. Commun. 11 (1) (2020) 1–7.
[19] S.W.X. Ong, Y.K. Tan, P.Y. Chia, T.H. Lee, O.T. Ng, M.S.Y. Wong, K. Marimuthu, Air, surface environmental, and personal protective equipment contamination by severe acute respiratory syndrome coronavirus 2 (SARS-CoV-2) from a symptomatic patient, J. Am. Med. Assoc. 323 (16) (2020) 1610–1612.
[20] C. Ma, A. Nikiforov, N. De Geyter, X. Dai, R. Morent, K.K. Ostrikov, Future antiviral polymers by plasma processing, Prog. Polym. Sci. 118 (2021), 101410.
[21] J.S. VanEpps, J.G. Younger, Implantable device related infection, Shock, Shock (Augusta, Ga.) 46 (6) (2016) 597–608.
[22] C.-E. Luyt, T. Sahnoun, M. Gautier, P. Vidal, S. Burrel, M. Pineton de Chambrun, J. Chommeloux, C. Desnos, J. Arzoine, A. Nieszkowska, Ventilator-associated pneumonia in patients with SARS-CoV-2-associated acute respiratory distress syndrome requiring ECMO: a retrospective cohort study, Ann. Intensive Care 10 (2020) 1–10.
[23] D.R. Giacobbe, D. Battaglini, E.M. Enrile, C. Dentone, A. Vena, C. Robba, L. Ball, M. Bartoletti, I. Coloretti, S. Di Bella, incidence and prognosis of ventilator-associated pneumonia in critically ill patients with COVID-19: a multicenter study, J. Clin. Med. 10 (4) (2021) 555.
[24] Y. Jiang, J. Xu, J. Lee, K. Du, E.-H. Yang, M.-W. Moon, C.-H. Choi, Nanotexturing of conjugated polymers via one-step maskless oxygen plasma etching for enhanced tunable wettability, Langmuir 33 (27) (2017) 6885–6894.
[25] T.-J. Ko, E.K. Her, B. Shin, H.-Y. Kim, K.-R. Lee, B.K. Hong, S.H. Kim, K.H. Oh, M.-W. Moon, Water condensation behavior on the surface of a network of superhydrophobic carbon fibers with high-aspect-ratio nanostructures, Carbon 50 (14) (2012) 5085–5092.
[26] J.P. Youngblood, T.J. McCarthy, Ultrahydrophobic polymer surfaces prepared by simultaneous ablation of polypropylene and sputtering of poly (tetrafluoroethylene) using radio frequency plasma, Macromolecules 32 (20) (1999) 6800–6806.
[27] I. Levchenko, S. Xu, O. Baranov, E.P. Ivanova, K. Bazaka, Plasma and polymers: recent progress and trends, Molecules 26 (13) (2021) 4091.
[28] A. Roy, K. Chatterjee, theoretical and computational investigations into mechanobactericidal activity of nanostructures at the bacteria-biomaterial interface: a critical review, Nanoscale 13 (2) (2021) 647–658.
[29] A. Velic, J. Hasan, Z. Li, P.K. Yarlagadda, Mechanics of bacterial interaction and death on nanopatterned surfaces, Biophys. J. 120 (2) (2021) 217–231.
[30] A. Epstein, A. Hochbaum, P. Kim, J. Aizenberg, Control of bacterial biofilm growth on surfaces by nanostructural mechanics and geometry, Nanotechnology 22 (49) (2011), 494007.
[31] R. Panowicz, M. Konarzewski, T. Durejko, M. Szala, M. Łazińska, M. Czerwińska, P. Prasuła, Properties of polyethylene terephthalate (PET) after thermo-oxidative aging, Materials 14 (14) (2021) 3833.
[32] Y. Bin, K. Oishi, K. Yoshida, M. Matsuo, Mechanical properties of poly (ethylene terephthalate) estimated in terms of orientation distribution of crystallites and amorphous chain segments under simultaneous biaxially stretching, Polym. J. 36 (11) (2004) 888–898.
[33] J. Xu, H. Moon, J. Xu, J. Lim, T. Fischer, H.A. McNally, H.O. Sintim, H. Lee, One-step large-scale nanotexturing of nonplanar PTFE surfaces to induce bactericidal and anti-inflammatory properties, ACS Appl. Mater. Interfaces 12 (24) (2020) 26893–26904.
[34] T.J. Ko, K.H. Oh, M.W. Moon, Plasma-Induced Hetero-Nanostructures on a polymer with selective metal Co-Deposition, Adv. Mater. Interfaces 2 (1) (2015) 1400431.
[35] K. Tsougeni, N. Vourdas, A. Tserepi, E. Gogolides, C. Cardinaud, Mechanisms of oxygen plasma nanotexturing of organic polymer surfaces: from stable super hydrophilic to super hydrophobic surfaces, Langmuir 25 (19) (2009) 11748–11759.
[36] A. Roy, K. Chatterjee, Bactericidal anisotropic nanostructures on titanium fabricated by maskless dry etching, ACS Applied Nano Materials 5 (3) (2022) 4447–4461.
[37] A. Roy, S.K. Gupta, S. Suwas, K. Chatterjee, The significance of crystallographic texture in dry etching of titanium to engineer bioinspired nanostructured bactericidal surfaces, JOM 74 (9) (2022) 3367–3378.
[38] C. Borcia, I. Punga, G. Borcia, Surface properties and hydrophobic recovery of polymers treated by atmospheric-pressure plasma, Appl. Surf. Sci. 317 (2014) 103–110.
[39] G. Primc, M. Mozetič, Hydrophobic recovery of Plasma-Hydrophilized polyethylene terephthalate polymers, Polymers 14 (12) (2022) 2496.
[40] I. Junkar, M. Modic, M. Mozeti, Modification of PET surface properties using extremely non-equilibrium oxygen plasma, Open Chem. 13 (1) (2015).
[41] D. Chandra, S. Yang, Stability of high-aspect-ratio micropillar arrays against adhesive and capillary forces, Acc. Chem. Res. 43 (8) (2010) 1080–1091.
[42] J.-H. Oh, M.-W. Moon, C.H. Park, Effect of crystallinity on the recovery rate of superhydrophobicity in plasma-nanostructured polymers, RSC Adv. 10 (18) (2020) 10939–10948.
[43] E.P. Ivanova, D.P. Linklater, M. Werner, V.A. Baulin, X. Xu, N. Vrancken, S. Rubanov, E. Hanssen, J. Wandiyanto, V.K. Truong, The multi-faceted mechano-bactericidal mechanism of nanostructured surfaces, Proc. Natl. Acad. Sci. 117 (23) (2020) 12598–12605.
[44] A. Elbourne, J. Chapman, A. Gelmi, D. Cozzolino, R.J. Crawford, V.K. Truong, Bacterial-nanostructure interactions: the role of cell elasticity and adhesion forces, J. Colloid Interface Sci. 546 (2019) 192–210.
[45] A. Valiei, N. Lin, G. McKay, D. Nguyen, C. Moraes, R.J. Hill, N. Tufenkji, Surface wettability is a key feature in the Mechano-Bactericidal activity of nanopillars, ACS Appl. Mater. Interfaces 14 (24) (2022) 27564–27574.
[46] A. Valiei, N. Lin, J.-F. Bryche, G. McKay, M. Canva, P.G. Charette, D. Nguyen, C. Moraes, N. Tufenkji, Hydrophilic mechano-bactericidal nanopillars require external forces to rapidly kill bacteria, Nano Lett. 20 (8) (2020) 5720–5727.
[47] S.M. Kim, J. Kim, S.M. Kang, S. Jang, D. Kang, S.E. Moon, H.N. Kim, H. Yoon, Directional clustering of slanted nanopillars by elastocapillarity, Small 12 (28) (2016) 3764–3769.
[48] W. Pajerski, J. Duch, D. Ochonska, M. Golda-Cepa, M. Brzychczy-Wloch, A. Kotarba, Bacterial attachment to oxygen-functionalized graphenic surfaces, Mater. Sci. Eng. C 113 (2020), 110972.
[49] R.S. Friedlander, H. Vlamakis, P. Kim, M. Khan, R. Kolter, J. Aizenberg, Bacterial flagella explore microscale hummocks and hollows to increase adhesion, Proc. Natl. Acad. Sci. 110 (14) (2013) 5624–5629.

[50] V.K. Truong, M. Al Kobaisi, K. Vasilev, D. Cozzolino, J. Chapman, current perspectives for engineering antimicrobial nanostructured materials, current opinion, Biomed. Eng. 23 (2022), 100399.
[51] C. Spengler, F. Nolle, J. Mischo, T. Faidt, S. Grandthyll, N. Thewes, M. Koch, F. Müller, M. Bischoff, M.A. Klatt, Strength of bacterial adhesion on nanostructured surfaces quantified by substrate morphometry, Nanoscale 11 (42) (2019) 19713–19722.
[52] N. Thewes, A. Thewes, P. Loskill, H. Peisker, M. Bischoff, M. Herrmann, L. Santen, K. Jacobs, Stochastic binding of staphylococcus aureus to hydrophobic surfaces, Soft Matter 11 (46) (2015) 8913–8919.
[53] M. Michalska, S.K. Laney, T. Li, M. Portnoi, N. Mordan, E. Allan, M.K. Tiwari, I. P. Parkin, I. Papakonstantinou, Bioinspired multifunctional glass surfaces through regenerative secondary mask lithography, Adv. Mater. 33 (43) (2021) 2102175.
[54] M. Michalska, R. Divan, P. Noirot, P.D. Laible, Antimicrobial properties of nanostructured surfaces–demonstrating the need for a standard testing methodology, Nanoscale 13 (41) (2021) 17603–17614.
[55] Z. Chen, Y. Gu, G. Wang, Q. Liu, Y. Li, Y. Weng, N. Lu, G. Yang, Y. Liu, Normal Force-Induced highly efficient mechanical sterilization of GaN nanopillars, Langmuir 38 (2) (2022) 856–862.
[56] M. Becce, A. Klöckner, S.G. Higgins, J. Penders, D. Hachim, C.J. Bashor, A. M. Edwards, M.M. Stevens, Assessing the impact of silicon nanowires on bacterial transformation and viability of escherichia coli, J. Mater. Chem. B 9 (24) (2021) 4906–4914.
[57] J. Jenkins, J. Mantell, C. Neal, A. Gholinia, P. Verkade, A.H. Nobbs, B. Su, Antibacterial effects of nanopillar surfaces are mediated by cell impedance, penetration and induction of oxidative stress, Nat. Commun. 11 (1) (2020) 1626.
[58] C.A. Dos Santos, G.R. Dos Santos, V.S. Soeiro, J.R. Dos Santos, M.d.A. Rebelo, M. V. Chaud, M. Gerenutti, D. Grotto, R. Pandit, M. Rai, Bacterial nanocellulose membranes combined with nisin: a strategy to prevent microbial growth, Cellulose 25 (2018) 6681–6689.
[59] A. Hayles, J. Hasan, R. Bright, J. Wood, D. Palms, P. Zilm, D. Barker, K. Vasilev, Spiked titanium nanostructures that inhibit anaerobic dental pathogens, ACS Applied Nano Materials 5 (9) (2022) 12051–12062.